Reynolds number effect on the bistable dynamic of a blunt-base bluff body

Yajun Fan [*] and Olivier Cadot

School of Engineering, University of Liverpool, Liverpool L69 3GH, United Kingdom

A three-dimensional blunt-base bluff body in a uniform flow is subjected to long-time stochastic dynamics of switching between two opposite wake states. This dynamic is investigated experimentally within the Reynolds number range Re $\simeq 10^4$–10^5. Long-time statistics coupled to a sensitivity analysis to the body attitude (defined as the pitch angle of the body with respect to the incoming flow) show that the wake switching rate decreases as Re increases. Equipping the body with passive roughness elements (turbulators) modifies the boundary layers before separation, seen as the inlet condition for the wake dynamic. Depending on their location and Re, the viscous sublayer length scale and the turbulent layer thickness can be modified independently. This sensitivity analysis to the inlet condition shows that a decrease of the viscous sublayer length scale at a given turbulent layer thickness leads to a decrease in the switching rate, whereas the modification of the turbulent layer thickness has almost no effect on the switching rate.

I. INTRODUCTION

There is a large variety of turbulent flows that undergo unpredictable and spectacular changes in their large-scale motion, thus provoking huge consequences, including the large overturn in the ocean [1], magnetic field reversals [2], multistability in the von Kármán flow [3] and Taylor-Couette system [4], Rayleigh-Bénard convection without [5,6] and with rotation [7], and wake switching of three-dimensional bluff bodies [8,9], among others. These sudden changes happen randomly and rarely, in that the waiting time before a change can be several orders of magnitude above the typical turbulent large-scale turnover time. It remains a fundamental challenge to understand and predict what triggers such large-scale motion changes within a turbulent background.

The present work focuses on the wake switching of three-dimensional bluff bodies. It is associated with a steady symmetry breaking that originates from a pitchfork bifurcation in the laminar regime at a Reynolds number of several hundred [10,11]. The wake steady instability persists through random bistable dynamics between the two asymmetric stable states until Reynolds numbers of at least few million [8]. Since the pioneering work in Ref. [10], the wake bistability has been studied experimentally and numerically (see, for instance, Refs. [12,13] and references therein).

In the turbulent regime, Ref. [8] reported a mean waiting time for the wake switching to be roughly inversely proportional to the free-stream velocity U_∞ and obtained $\tau = 1472H/U_\infty$ for a Reynolds number Re $= \frac{U_\infty H}{\nu} = 9.2 \times 10^4$ where H is the body height and ν is the air kinematic viscosity. Later, Ref. [14] investigated two different Reynolds numbers and found $\tau = 1418H/U_\infty$ at Re $= 7.7\times10^5$ and $\tau = 1092H/U_\infty$ at Re $= 5.1\times10^5$. Although both

experiments are not comparable because of their different ground clearance, they provide similar orders of magnitude. Interestingly, Ref. [14] shows a reduction of the occurrence of the wake switching as the Reynolds numbers is increased. Recent studies investigated the effect of the free-stream turbulence intensity on the switching occurrence. Reference [12] found the switching rate to increase proportionally to the turbulence intensity, ranging from 1% to 16% at Re $= 2.9\times10^5$. Previously, Ref. [15] reported a slight decrease of the switching rate at a lower Reynolds number Re $= 8 \times 10^4$, but when the turbulence intensity was only increased to 5.6% from 1.8%. In addition to their Reynolds numbers, the different characteristic length scales of the incoming turbulence in these two works may also contribute to their different conclusions.

One may wonder about the effect of the turbulent modelling choice on the switching rate simulation. The first wake switching was observed in Ref. [16] with an Large Eddy Simulation (LES) and then reproduced in other simulations [17–19]. In particular, Ref. [19] pointed out the role of the front separated bubbles to trigger the wake switching by shedding large hairpin vortices. Although the Improved Delayed Detached Eddy Simulation (IDDES) simulation of Ref. [17] does not capture the front separation bubble, where incoming turbulence is introduced with a synthetic eddy method [20] it reproduces a similar occurrence of switching events as in the experiment. Reference [18] build a low-dimensional model based on their Direct Numerical Simulation (DNS) of the flow. The chaotic model produces random switches with characteristic timescales, in agreement with the simulation and experiments, and suggests that random switches are triggered by the increase of the vortex shedding activity in the wake. There is then no clear identification for the cause of the wake switching. The aim of the present work focuses on the switching rate: How does it evolve with the Reynolds number and to which part of the flow is it sensitive?

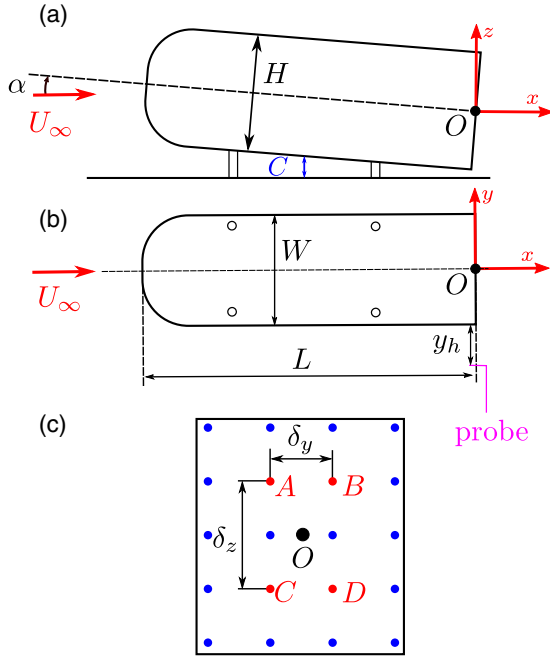*Yajun.Fan@liverpool.ac.uk

(a)

(b)

(c)

FIG. 1. Experimental setup: side (a), top (b), and back (c) views of the model. Base with pressure taps location (c) marked as red and blue filled circles.

The strategy is twofold: first, to investigate a Reynolds number range of Re $\simeq 10^4$–10^5 together with a sensitivity analysis of body pitch attitude variations, and second, to manipulate the boundary layer upstream the wake in order to obtain different conditions at the trailing edge separation. The manipulation is realized by the placement of passive roughness elements (sawtooth stripes called turbulators) on different parts of the body. It will be shown that (i) the switching rate decreases with the Reynolds number, thus confirming the former result of Ref. [14], and (ii) the large velocity gradient in the viscous sublayer thickness influences the switching rate.

The paper is organized as follows. The experimental setup and measurement techniques are described in Sec. II. In particular, Sec. II C gives the detail concerning the sawtooth turbulator which is used to modify the development of the boundary layer along the body, as well as its effect on the front separation bubble. A definition of the wake switching event is provided in Sec. III. Results in Sec. IV present the effect of the Reynolds number and turbulator on the wake switching occurrence in relationship to the boundary layer at the trailing edge. Section V discusses the results and concludes the work, offering a perspective on future research.

II. EXPERIMENTAL SETUP

The flat back Ahmed model (see Fig. 1) and the wind tunnel are identical to those in Ref. [21], in which the experimental setup is fully detailed. Briefly, the model has dimensions $L = 560$ mm, $W = 180$ mm, and $H = 200$ mm. It is supported by four cylinders 15 mm in diameter, leaving a clearance of $C = 20$ mm. The radius of the rounding of the forebody is 70 mm. The rectangular base in Fig. 1(b) is taller than wide, with the aspect ratio $H/W = 1.11$. The

front and rear axles are positioned with a precision of 1μm, achieving the accurate control of the pitch angle α, as defined in Fig. 1(a).

Experiments are carried out in a blowing wind tunnel having a test section 1.2 m wide by 0.6 m high and 2.4 m long. The free-stream turbulence intensity is 1% and the blockage ratio is 4.9%. When the body is not in the test section, the ground boundary layer thickness based on 99% of the free-stream velocity is $\delta_{99} = 9$ mm at the location of the front of the body. Experiments are conducted at five different velocities $U_\infty = [5.7, 7.0, 10.5, 15.6, 22.9]$ m/s, leading to Reynolds numbers Re $= U_\infty H/\nu$ varying from Re $= 7.7 \times 10^4$ to Re $= 3.1 \times 10^5$. The body height H and free-stream velocity U_∞ are chosen as scaling units, and any quantity a^* with an asterisk in the following represents the corresponding nondimensional value of a.

A. Pressure measurement

There are 20 pressure taps equally spaced at the base [see Fig. 1(c)]. The pressure is measured with a Scanivalve ZOC33/64PX pressure scanner placed inside the body. The sampling frequency is 1 kHz per channel. The static pressure p_∞ of the test section is used to compute the instantaneous pressure coefficient $c_p = (p - p_\infty)/q_\infty$, where q_∞ is the dynamic pressure. The base pressure gradient, shown in previous research [8] to be an appropriate instantaneous indicator for the wake asymmetry, is estimated as in Ref. [21], where the dimensionless pressure gradient in the vertical direction $g_z = \frac{H}{2\delta_z}[(c_{p_A} + c_{p_B}) - (c_{p_C} + c_{p_D})]$ is simply computed using the four pressure taps denoted by A, B, C, D in Fig. 1(b). The base suction coefficient

$$c_b = -\frac{1}{HW} \iint c_p ds \qquad (1)$$

is computed from the spatial average of the 20 pressure taps at the base. The pressure signal is recorded during the acquisition time $t_{acq} = t^*_{acq} \frac{H}{U_\infty}$ with $t^*_{acq} = 1.6 \times 10^5$ equivalent to 5600 s at the lowest free-stream velocity and to 1400 s at the largest, which appeared large enough to achieve converged wake switching event statistics.

B. Velocity measurement

The velocity in the boundary layer developing along the body is measured by means of hot-wire anemometers (HWA) from DANTEC (hot-wire type 55P15, support type 55H22). The probe is mounted on a two-dimensional (2D) displacement system consisting of two Standa motorized translation stages (8MT195/8MT50) having a precision of 1μm. The wire is oriented to be essentially sensitive to the modulus of the streamwise velocity denoted by u. The distance from the body surface to the probe is defined as y_h, as shown in Fig. 1(b). For each location, two velocity profiles along the normal direction of the body wall are explored: The first one goes through the whole boundary layer, with an acquisition time of 20 s and a displacement step of 0.5 mm; the second one focuses on the viscous sublayer, with an acquisition time of 40 s and a displacement step of 0.1 mm. For both cases the sampling frequency is 1 kHz. Finally, the mean $U = \bar{u}$ and the
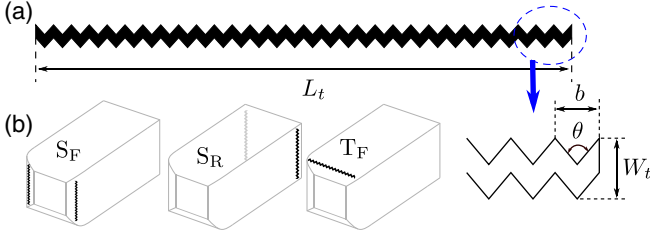
FIG. 2. Turbulator geometry (a) and model configurations with turbulators (b).

fluctuations $U' = (\overline{(u - \overline{u})^2})^{\frac{1}{2}}$ are extracted from the data and plotted versus y_h. The viscous sublayer length scale is defined as [22]

$$\delta_\nu = \left(\frac{\nu}{dU/dy_h|_{y_h=0}} \right)^{\frac{1}{2}}. \qquad (2)$$

The velocity profile slope in the denominator is computed from the data point the closest to the wall (approximately 100μm) and the extrapolated position of the wall obtained at the lowest Reynolds number. The accuracy of δ_ν that will be displayed by error bars is obtained from the uncertainty on the exact wall position estimated to be ±10μm.

C. Turbulator

A sawtooth turbulator manufactured from high-impact polystyrene sheets [see Fig. 1(a)] is used to modify the development of the boundary layer along the body to provide some different wake inflow conditions at the base. Its length, width, and thickness are respectively $L_t = 180$ mm, $W_t = 10$ mm, and 1.0 mm. The sawtooth geometry is given by $\theta = 60°$ and $b = 6$ mm. As shown in Fig. 2(b), three model configurations are chosen for the turbulators placement: a lateral pair at the forebody (S_F) with their trailing edge at $x = -490$ mm [equivalently $x_f^* = 0$ in Fig. 3(d)] or at the rear (S_R) at $x = -10$ mm and a top single turbulator at the forebody (T_F) at $x = -490$ mm.

The forebody configurations are made to modify the separation bubbles at the nose-body junction reported experimentally in Refs. [8,17,19]. The bubble on the lateral side is surveyed using the HWA as described above for Re $= 9.5 \times 10^4$ in Figs. 3(a) and 3(b) and Re $= 2.1 \times 10^5$ in Figs. 3(c) and 3(d). The bubble of the baseline (no turbulators) represented with black symbols in Fig. 3 is clearly identifiable at Re $= 9.5 \times 10^4$ in Fig. 3(a) with a high shear moving away from the wall due to the separation. Increasing the Reynolds number to Re $= 2.1 \times 10^5$ reduces considerably the bubble size, as can be seen in Fig. 3(c). The turbulator placed in front of the separation has the opposite effect (shown with red symbols) depending on the Reynolds number; it reduces the bubble size at low Reynolds number [Fig. 3(a)], decreasing the velocity fluctuation in the boundary layer [Fig. 3(b)]. At the larger Reynolds number, it increases the bubble size by a factor close to 2 [Fig. 3(c)] and increases the velocity fluctuation in the boundary layer [Fig. 3(d)].
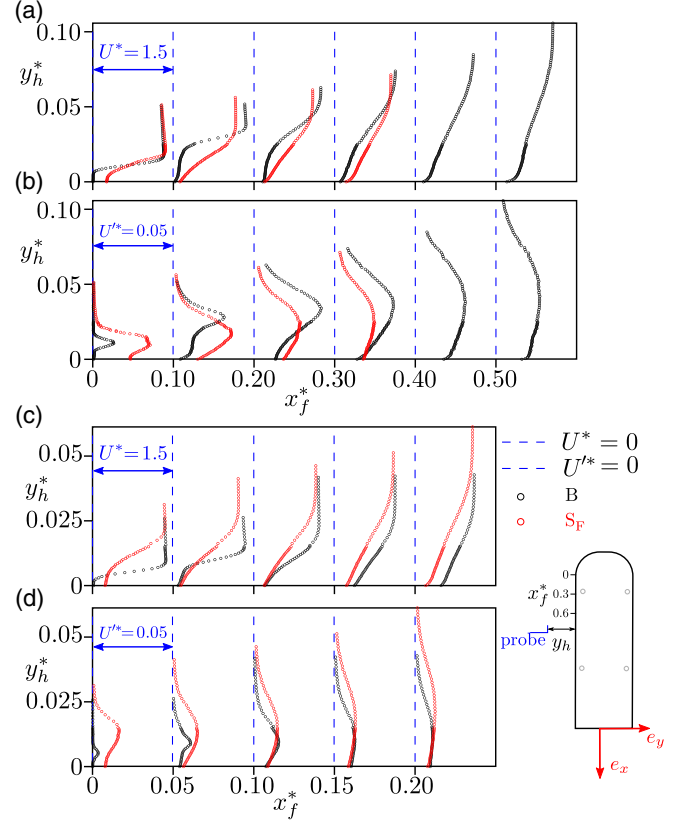

FIG. 3. Forebody bubble separation on the lateral wall at Re $= 9.5 \times 10^4$ [(a), (b)] and Re $= 2.1 \times 10^5$ [(c), (d)]. Mean [(a), (c)] and fluctuating [(b), (d)] velocity profiles for the baseline (black symbols) and turbulators placed in the S_F configuration [see Fig. 2(b)].

III. SWITCHING EVENT DEFINITION

In this section, we define how a switching event is detected from the base pressure gradient signal, of which a sample is shown in Fig. 4(a) for $U_\infty = 15.6$ m/s. The gradient is first low pass filtered with a cutoff frequency that depends on the free-stream velocity, $f_{filter} = f_{filter}^* U_\infty / H$ with $f_{filter}^* = 0.064$. These cutoff frequencies are shown with vertical arrows in Fig. 4(b), which presents the power spectrum density of the pressure read at the tap B [see Fig. 1(b)] for the five free-stream velocities. The filtered gradient $g_z^{filter}(t)$ is shown in Fig. 4(a) with the red line.

The probability P^+ (resp. P^-) of observing a positive (resp. negative) gradient is simply obtained by summing the positive (resp. negative) part of the probability density function of g_z^{filter}. As shown in Fig. 4(c), the observed state is sensitive to the pitch attitude, and we define as α_0 the pitch angle when $P^+ = P^-$. These probabilities will be referred to as wake state probability for simplicity for the remainder of the paper.

To define a switching event, we use a threshold r such that $|g_z| < r$ implies that the wake is in a transient dynamics, and otherwise implies that the wake is in a state. A switching event corresponds to a gradient of an initial state that enters the transient dynamics and evolves toward the opposite state, or in other words penetrates the stripe of width $2r$ displayed with the two gray solid lines in Fig. 4(a) and then exits the stripe on
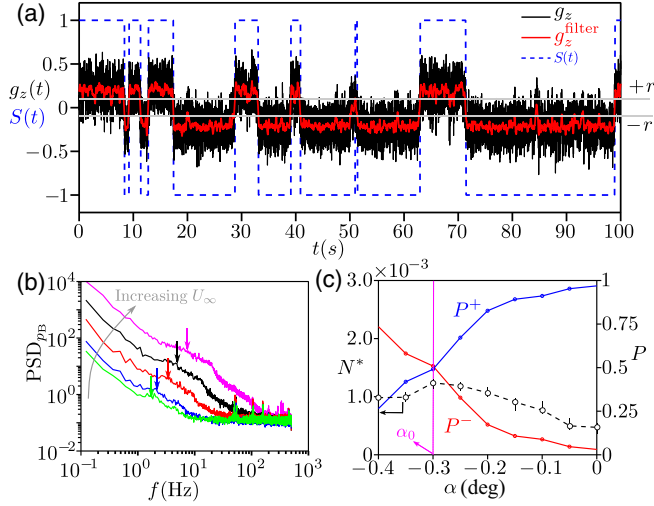
FIG. 4. Signal processing for switching events detection. Time series (a) of the gradient $g_z(t)$, filtered gradient $g_z^{\text{filter}}(t)$, and state function $S(t)$ computed from the threshold r (see text). Power spectrum density (b), PSD of the pressure read at the tap B [see Fig. 1(c)]. Vertical arrows in panel (b) indicate the low pass cutoff frequency at $f_{\text{filter}}^* = 0.064$ for each U_∞. (c) Switching rate N^* and probability P vs the pitch α computed from the pressure signals at $U_\infty = 15.6$ m/s.

the opposite side. This is achieved by the following algorithm:

$$S(t) = \begin{cases} -1 & \text{if } g_z^{\text{filter}}(t) < -r \\ S(t - \delta t) & \text{if } \left| g_z^{\text{filter}}(t) \right| \leqslant r \\ 1 & \text{if } g_z^{\text{filter}}(t) > r, \end{cases} \quad (3)$$

where δt is the acquisition sampling time. The resulting state function $S(t)$ is represented by the dashed blue line in Fig. 4(a), and a switching event is detected by the change of sign of the state function. The dimensionless switching rate $N^* = N/t_{\text{acq}}^*$ is calculated by counting the number N of switching events during the dimensionless acquisition time $t_{\text{acq}}^* = 1.6 \times 10^5$. Although the value of the threshold r is arbitrary, the switching rate that obviously decreases when r increases becomes quite insensitive to the threshold when $0.1 < r < 0.2$. Thus, we have chosen the value $r = 0.15$ displayed in Fig. 4(a). The indicative error bars showed for N^* are obtained from the extreme values $r = 0.1$ and $r = 0.2$ of the threshold.

IV. RESULTS

We perform various tests by changing the free-stream velocity or by adding turbulators on the body. For each test, wake switching events are counted as described above and the corresponding flow is characterized by the boundary layer properties prior base separation, seen as the inflow condition for the wake dynamics. As such, the velocity profile on a vertical side at mid-height and 1 mm upstream of the salient edge, as depicted in Fig. 1(b), is used to define this inflow condition.

The plain body (no turbulators) is first considered. The Reynolds number effect is clearly identified in the mean U^* and fluctuating U'^* velocity profiles in Fig. 5 of the boundary layer at the base separation. They all correspond to turbulent
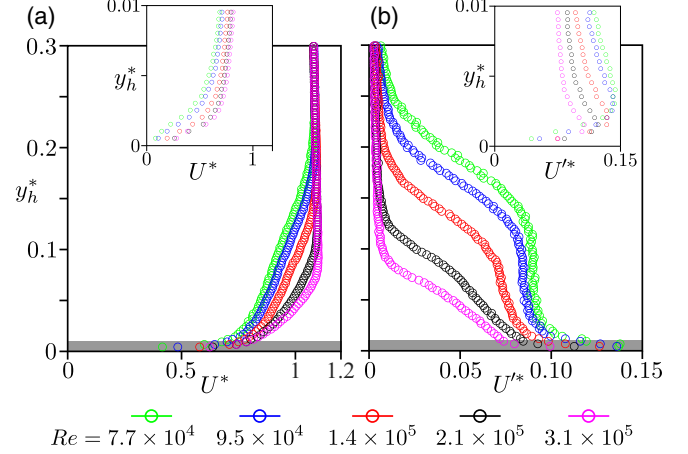

FIG. 5. Reynolds number effect on the boundary layer prior to the base separation: Mean (a) and fluctuating (b) velocity profiles vs the normal wall coordinate y_h at $(x = -1$ mm, $y = -W/2 - y_h, z = 0)$. The insets are enlargements of the region close to the wall highlighted by the gray area.

boundary layers whose δ_{99} thickness decreases with increasing Re up to a factor of approximately 2.5 between the lowest and largest Re in Fig. 5(a). The simultaneous thinning of the viscous sublayer with Re is measurable in the inset of Fig. 5(a). The mean velocity decrease is associated with fluctuations that globally decreases with increasing Re [Fig. 5(b)] as can be seen in the inset of Fig. 5(b). Figure 6 shows how different inflow conditions are correlated to the wake switching statistics. The bistable dynamics observed during the wake transitions between a permanently positive to permanently negative vertical gradient [21] is always observed in a typical range of pitch of $0.6°$ as shown in Fig. 6(a) but the pitch α_0 at which both wake orientations are equally explored depends clearly on Re, as shown by the inset of Fig. 6(a). There is no observable trend with Re in the curves shown in Fig. 6(a), but the switching rate measured over the pitch range in Fig. 6(b) reveals a clear Re hierarchy where the lower switching rate corresponds to higher Reynolds number. The inset in Fig. 6(b) shows this variation considering the switching rate N_0^* at which both wake orientations are equally explored.

The question of why the switching rate decreases with Reynolds number is now addressed with the S_R and S_F turbulator configurations illustrated in Fig. 2(b). These two configurations are tested for the Reynolds numbers Re $= 9.5 \times 10^4$ and Re $= 2.1 \times 10^5$ in Fig. 7. The idea is to study whether the switching rate is sensitive with changes of incoming turbulent fluctuation or with changes of the strong shear in the viscous sublayer. The new inflow conditions are shown in Fig. 7 for the S_F (blue color) and S_R (red color) configurations. The only configuration that clearly modifies the switching rate is observed for the low Reynolds number (Re $= 9.5 \times 10^4$) in Fig. 8(a). It corresponds to the turbulators at the rear (S_R) for which δ_{99}, measurable in Figs. 7(a) and 7(b), is identical to the baseline (no turbulator, same Re) but with a significantly smaller viscous sublayer length scale as shown by the insets. It has to be mentioned that a configuration with turbulators on the four rear sides at Re $= 9.5 \times 10^4$ (not shown here) did not
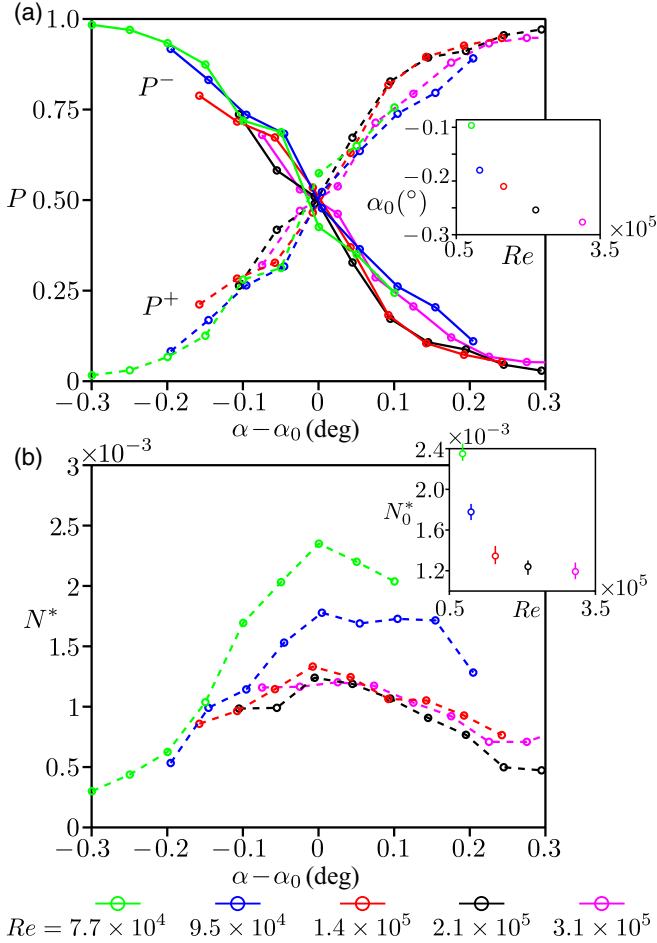
FIG. 6. Statistical properties of the bistable wake dynamic as a function of the Reynolds numbers: wake state probabilities (a) vs pitch attitudes and required pitch for equal wake state probability [inset of panel (a)]. Switching rate N^* (b) vs pitch attitudes and switching rate at equal wake state probability [inset of panel (b)].

FIG. 7. Turbulators' effect on the boundary layer prior to the base separation in the S_F (blue symbols) and S_R (red symbols) configurations (see Fig. 2) at $Re = 9.5 \times 10^4$ [(a), (b)] and $Re = 2.1 \times 10^5$ [(c), (d)]. Mean [(a), (c)] and fluctuating [(b), (d)] velocity profiles vs the normal wall coordinate y_h at ($x = -1$ mm, $y = -W/2 - y_h$, $z = 0$). The insets are enlargements of the region close to the wall highlighted by the gray area.

lead to any further decrease of the switching rate than the S_R configuration. For the three other cases [S_F in Fig. 8(a) and S_R, S_F in Fig. 8(b)], albeit the drastic changes of δ_{99} and the fluctuations, there is surprisingly no change in the switching rate. It is remarkable that for all of these three configurations the viscous sublayers are observed to remain the same as for the baseline.

Measurements of the viscous sublayer length scale are extracted using Eq. (2) from the mean velocity profiles at mid-height of the lateral side trailing edge (those shown in Figs. 5 and 7). This length scale is referred to as δ_ν^S. Velocity profiles at mid-width of the top side trailing edge, $U(x = -1$ mm, $y = 0, z = H/2 + z_h)$ have also been taken but they are not shown. The corresponding viscous sublayer thickness will be denoted δ_ν^T. It is observed that this top side boundary layer remains unchanged when turbulators are placed on the lateral side of the body in both configurations S_F and S_R. We now consider a new case for the lowest Reynolds number $Re = 7.7 \times 10^4$ with one turbulator at the front top side [configuration T_F in Fig. 2(b)]. This turbulator reduces the separated front bubble as described in Sec. II C and Fig. 3(a). It also produces the same inflow change as for the S_F configuration in Figs. 7(a)
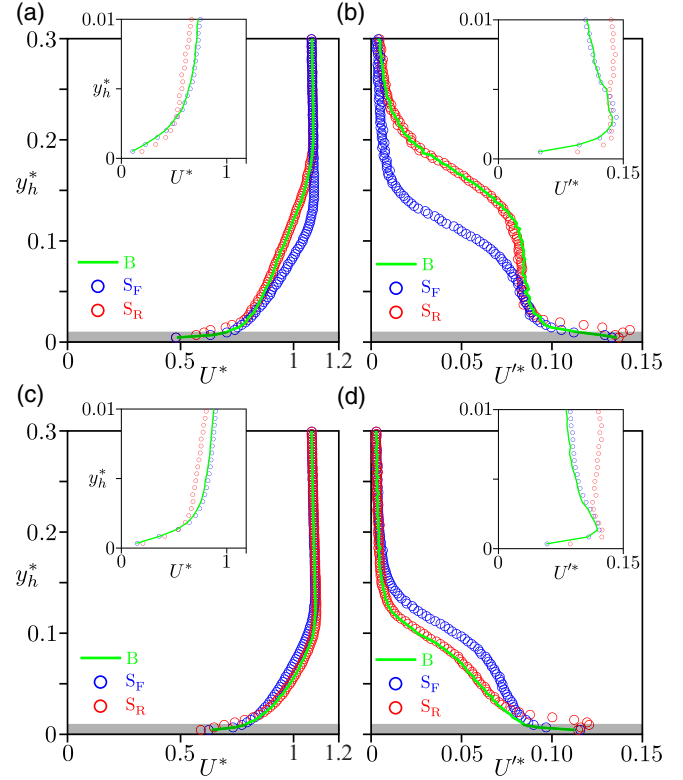
and 7(b) with a reduction of δ_{99} and fluctuations, but at the top edge of the base.

The viscous sublayer length scale δ_ν and the boundary layer thickness δ_{99} of both the lateral and top sides for the baseline are plotted with open circles in Figs. 9(a) and 9(b). As expected from the previous observations about the velocity profiles, both are decreasing with the Reynolds number. Compared to the top side thickness δ_ν^{T*}, there seems to be a saturation of the lateral side thickness δ_ν^{S*} for the largest Reynolds numbers at 3.1×10^5. It is attributed to a lateral vibration of the model caused by the elasticity of the mounting system. A laser sensor head (LK-G402 from Keyence) has been used to measure the rms displacement fluctuation of the wall of the lateral boundary layer. It was found to increase as U_∞ increases and to reach 8 μm for the experiment at $Re = 3.1 \times 10^5$, consistent with the observed saturation. However, this effect does not affect all results obtained at lower Re for the lateral side boundary layer.

Figure 9(a) confirms the decrease of the sublayer length scale in the S_R configuration (diamond symbols), especially at $Re = 9.5 \times 10^4$, while there is almost no change for all other turbulator configurations, including the S_F and T_F shown as the black cross symbol and red star symbol. It can be seen in Fig. 9(b) that front turbulators are able to decrease or increase the thickness δ_{99} depending on the Reynolds number,
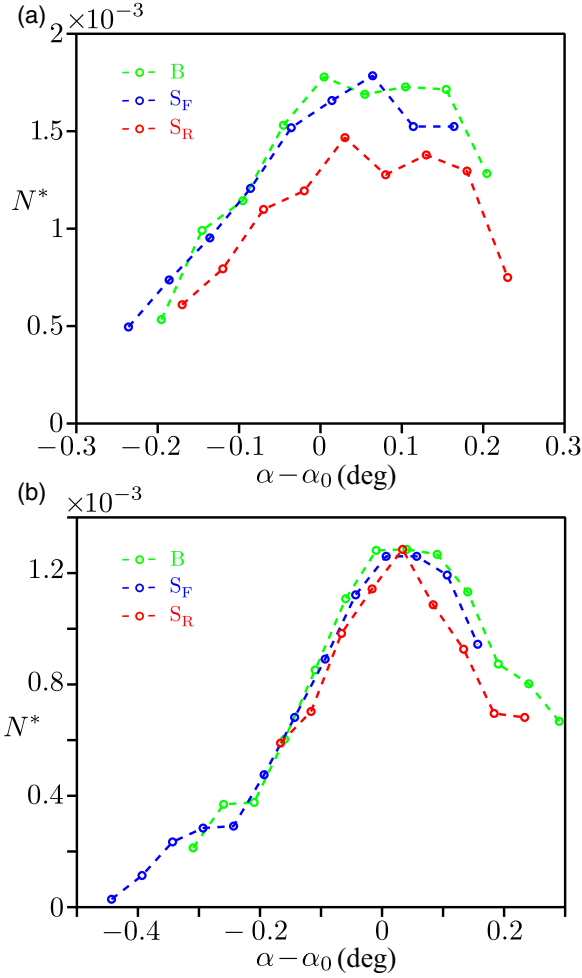
FIG. 8. Switching rate N^* vs pitch attitudes for different turbulator configurations S_F, S_R [see Fig. 2(b)] at two Reynolds numbers: $Re = 9.5 \times 10^4$ (a) and $Re = 2.1 \times 10^5$ (b).

FIG. 9. Viscous sublayer length scale δ_ν^* (a) as defined in Eq. (2) and the boundary thickness δ_{99}^* (b) vs Re for the lateral side, δ_ν^{S*} (black symbols) measured at $(x = -1 \text{ mm}, y = -W/2, z = 0)$ and the top side, δ_ν^{T*} (red symbols) measured at $(x = -1 \text{ mm}, y = 0, z = H/2)$. Switching rate [(c), (d)] at equal states probability vs the lateral side viscous sublayer length scale (c) δ_ν^{S*} and the lateral boundary thickness δ_{99}^* (d). The baseline measurements are shown as open circle symbols and turbulator configurations S_F, S_R, and T_F [see Fig. 2(b)] as cross, diamond, and star symbols respectively.

while the rear turbulator has almost no effect. The plot in Fig. 9(c) summarizes the main finding of this work which is the satisfactory relationship between the switching rate at equal wake state probability and the viscous sublayer length scale at the lateral side wall for the baseline and all turbulator configurations. In contrast, such a relationship cannot be built between the switching rate N_0^* and the boundary layer thickness δ_{99}^*, as shown in Fig. 9(d).

V. DISCUSSION AND CONCLUSION

The wake steady instability of the flat-back Ahmed body, widely reported in the literature, manifests as a stochastic switching between two stable states. The effect of the Reynolds number on the switching rate is investigated in a moderate range of about half a decade. A significant decrease of the switching rate by a factor of two is observed when the Reynolds number increases from 7.7×10^4 to 3.1×10^5. The decreasing trends of the switching rate confirmed the previous observation of Ref. [14] with only two data points.

The present results point out the sensitivity of the occurrence of the wake switching events to the turbulent boundary layer viscous sublayer prior to the base separation. It is found
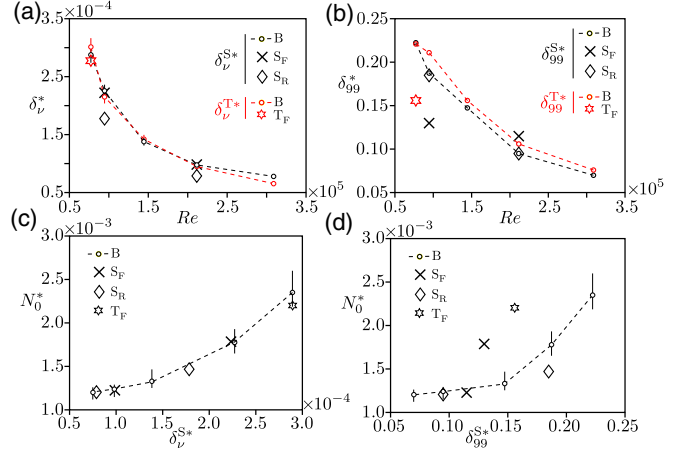
that the thinner viscous sublayer at separation, resulting from either the increase of the Reynolds number or the turbulator placement, corresponds to lower switching rate. It could be anticipated that the wake steady instability is strengthened by the viscous sublayer length decrease. This instability results from the global interaction of the vorticity contained in the free shear layers through the Biot-Savart law [23], of which a thinning implies a vorticity or velocity gradient amplification. This amplification may reinforce the stability of the equilibrium states, making the turbulent fluctuation less efficient to trigger a transition from one state to the other. This strengthening of the stability can be indicated by the mean base suction C_b [Eq. (1)]. As shown in Fig. 10, a larger base suction C_b is observed when the switching rate is reduced either by increasing the Reynolds number of the baseline (dashed line) or placing turbulators in the S_R configuration at $Re = 9.5 \times 10^4$ (red diamond symbol at $C_b = 0.24$). All other cases of turbulator configurations for which the base suction
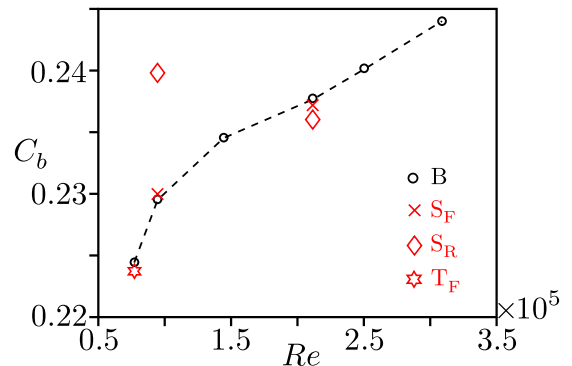

FIG. 10. Base pressure drag measured at $\alpha = \alpha_0$ vs Reynolds number and turbulator configurations.

remains similar to the dashed line baseline do not correspond to any change of the switching rate.

The study also reveals, by means of turbulator placements on the body, that the switching rate is not sensitive to the turbulent fluctuation magnitude contained in the modified boundary layer prior to the base separation. This might be an indication that fluctuations should be coherent over a given scale to trigger a wake switching event, which is never achieved in the turbulent content of the boundary layer for the presented experiment. This was likely the case in Ref. [19], which used different turbulent modeling and proposed that the front separation bubble is a key element to trigger the switching event. In the present case, the suppression or enhancement of the separation bubble realized through the placement of the turbulator has almost no impact on the switching rate. Although our experiment clearly shows the effect of the viscous sublayer length scale, the relationship between the wake switching event and the turbulent fluctuation within the boundary layer is still an open question.

The study should be extended over a wider Reynolds number range toward the laminar regime. At the threshold of the steady instability, the switching rate is expected to tend to zero. Thus, to agree with the present study, the switching rate should then go through a maximum as the Reynolds number decreases. A wide range of Reynolds numbers would imply experimentally a change of the model scale and/or working fluids. The incoming boundary layer on the ground should also be adapted to the model scale. The later experimental difficulty could be avoided considering the body with no ground proximity and supports such as having a uniform incoming flow as proposed in the experiment of Ref. [24].

[1] D. Castellana, S. Baars, F. W. Wubs, and H. A. Dijkstra, Transition probabilities of noise-induced transitions of the Atlantic Ocean circulation, Sci. Rep. **9**, 20284 (2019).

[2] M. Berhanu, R. Monchaux, S. Fauve, N. Mordant, F. Pétrélis, A. Chiffaudel, F. Daviaud, B. Dubrulle, L. Marié, F. Ravelet, M. Bourgoin, P. Odier, J.-F. Pinton, and R. Volk, Magnetic field reversals in an experimental turbulent dynamo, EPL **77**, 59001 (2007).

[3] P.-P. Cortet, E. Herbert, A. Chiffaudel, F. Daviaud, B. Dubrulle, and V. Padilla, Susceptibility divergence, phase transition, and multistability of a highly turbulent closed flow, J. Stat. Mech. Theory Exp. (2011) P07012.

[4] S. G. Huisman, R. C. van der Veen, C. Sun, and D. Lohse, Multiple states in highly turbulent Taylor-Couette flow, Nat. Commun. **5**, 3820(2014).

[5] H.-D. Xi and K.-Q. Xia, Flow mode transitions in turbulent thermal convection, Phys. Fluids **20**, 055104 (2008).

[6] B. Podvin and A. Sergent, Precursor for wind reversal in a square Rayleigh-Bénard cell, Phys. Rev. E **95**, 013112 (2017).

[7] P. Wei, S. Weiss, and G. Ahlers, Multiple Transitions in Rotating Turbulent Rayleigh-Bénard Convection, Phys. Rev. Lett. **114**, 114506 (2015).

[8] M. Grandemange, M. Gohlke, and O. Cadot, Turbulent wake past a three-dimensional blunt body. Part 1. Global modes and bi-stability, J. Fluid Mech. **722**, 51 (2013).

[9] G. Rigas, A. Oxlade, A. Morgans, and J. Morrison, Low-dimensional dynamics of a turbulent axisymmetric wake, J. Fluid Mech. **755**, R5 (2014).

[10] M. Grandemange, O. Cadot, and M. Gohlke, Reflectional symmetry breaking of the separated flow over three-dimensional bluff bodies, Phys. Rev. E **86**, 035302(R) (2012).

[11] O. Evstafyeva, A. S. Morgans, and L. Dalla Longa, Simulation and feedback control of the Ahmed body flow exhibiting symmetry breaking behaviour, J. Fluid Mech. **817**, R2 (2017).

[12] D. Burton, S. Wang, D. T. Smith, H. N. Scott, T. N. Crouch, and M. C. Thompson, The influence of background turbulence on Ahmed-body wake bistability, J. Fluid Mech. **926**, R1 (2021).

[13] D. Ahmed and A. Morgans, Nonlinear feedback control of bimodality in the wake of a three-dimensional bluff body, Phys. Rev. Fluids **7**, 084401 (2022).

[14] R. Volpe, P. Devinant, and A. Kourta, Experimental characterization of the unsteady natural wake of the full-scale square back Ahmed body: Flow bi-stability and spectral analysis, Exp. Fluids **56**, 99 (2015).

[15] O. Cadot, M. Almarzooqi, A. Legeai, V. Parezanović, and L. Pastur, On three-dimensional bluff body wake symmetry breaking with free-stream turbulence and residual asymmetry, Compt. Ren. Mécanique **348**, 509 (2020).

[16] L. Dalla Longa, O. Evstafyeva, and A. Morgans, Simulations of the bi-modal wake past three-dimensional blunt bluff bodies, J. Fluid Mech. **866**, 791 (2019).

[17] Y. Fan, C. Xia, S. Chu, Z. Yang, and O. Cadot, Experimental and numerical analysis of the bi-stable turbulent wake of a rectangular flat-backed bluff body, Phys. Fluids **32**, 105111 (2020).

[18] B. Podvin, S. Pellerin, Y. Fraigneau, G. Bonnavion, and O. Cadot, Low-order modelling of the wake dynamics of an Ahmed body, J. Fluid Mech. **927**, R6 (2021).

[19] F. Hesse and A.-S. Morgans, Simulation of wake bimodality behind squareback bluff bodies using LES, Comp. Fluids **223**, 104901 (2021).

[20] N. Jarrin, S. Benhamadouche, D. Laurence, and R. Prosser, A synthetic-eddy method for generating inflow conditions for large-eddy simulations, Int. J. Heat Fluid Flow **27**, 585 (2006).

[21] Y. Fan, V. Parezanović, and O. Cadot, Wake transitions and steady z-instability of an Ahmed body in varying flow conditions, J. Fluid Mech. **942**, A22 (2022).

[22] H. Schlichting and K. Gersten, *Boundary-Layer Theory* (Springer, Berlin, 2016).

[23] P. Saffman, *Vortex Dynamics* (Cambridge University Press, Cambridge, UK, 1992).

[24] A. Legeai and O. Cadot, On the recirculating flow of three-dimensional asymmetric bluff bodies, Exp. Fluids **61**, 249 (2020).